Open Access

Journal of Energy and Power Technology

LIDSEN Publishing Inc.

Short Report

A Dual-PRF Scan Mode and Adaptive Doppler-Velocity Dealiasing to Increase Radar Clear-Air Velocity Data Coverage and Usability

Qin Xu [1, *], Kang Nai [1, 2], Valery Melnikov [1, 2]

1. NOAA/OAR/National Severe Storms Laboratory (NSSL), Norman, Oklahoma, USA; E-Mails: Qin.Xu@noaa.gov; kang.nai@noaa.gov; valery.melnikov@noaa.gov
2. Cooperative Institute for Severe and High-Impact Weather Research and Operations, University of Oklahoma, Norman, Oklahoma, USA

* **Correspondence:** Qin Xu; E-Mail: Qin.Xu@noaa.gov

Academic Editor: Andrés Elías Feijóo Lorenzo

Collection: Wind Energy

Journal of Energy and Power Technology
2022, volume 4, issue 4
doi:10.21926/jept.2204034

Received: August 05, 2022
Accepted: October 10, 2022
Published: October 13, 2022

Abstract

By using long pulses with extended dwelling time, lowered pulse repetition frequency (PRF) and reduced Nyquist velocity, the radar measurement capability can be enhanced to increase clear-air Doppler velocity data coverage (which is beneficial for radar wind analysis and data assimilation and motivated our previous study). This potential capability is further explored (beyond our previous study) by not only modifying the existing operational clear-air scan mode with a lowered PRF and reduced the Nyquist velocity (to nearly 12 m/s) but also coupling this low-PRF scan with a high-PRF scan into a new dual-PRF scan mode. With this dual-PRF scan mode, the velocities from the high-PRF scan can be used to dealias the raw velocities from the low-PRF scan. Doppler velocities collected by using the low-PRF scan in this dual-PRF scan mode exhibit enhanced clear-air data coverage but encounter increased difficulties in dealiasing beyond the radial range covered by the high-PRF scan. To overcome the encountered difficulties, the previously developed alias-robust variational method for analyzing severely aliased radar velocity observations with small Nyquist velocities is further improved adaptively, so reliable reference radial velocities can be obtained and used to

dealias the low-PRF scanned raw velocities on range circles beyond those covered by the high-PRF scan.

Keywords
Radar; dual-PRF scan mode; clear-air; data coverage; velocity dealiasing

1. Introduction

The network of Weather Surveillance Radar-1988 Doppler (WSR-88D) systems in the United States has played a critical role in improving short-range forecasts and warnings for severe thunderstorms, tornadoes, and flash floods [1-8]. In addition, high-resolution reflectivity and velocity observations have been ingested not only into the operational data assimilation systems to improve numerical weather predictions [9, 10] but also into the NSSL experimental Warn-on-Forecast system to improve short-term ensemble predictions of severe thunderstorms and flash floods [11-14]. However, NEXRAD velocity data collected under clear-air weather conditions have not found much usage due to shallow and limited radial-range coverage (≤50 km) in clear air and the relatively large spacing between radars (≈300 km). Ideally and in principle, the clear-air velocity observations can be assimilated directly (with adequate data quality control) to improve numerical weather predictions especially if their spatial coverage can be enhanced. This has motivated our recent study [15] to explore how the existing scan modes used for clear-air by the WSR-88Ds can be modified to enhance the detectability and thus increase the coverage of velocity observations. This paper reports a new research progress beyond the study of Xu et al. [15].

It is well known that using long pulses with extended dwell time can enhance radar sensitivity and thus increase clear-air Doppler velocity data coverage, and this can provide additional information for radar wind analysis and data assimilation. This potential capability was first explored in Xu et al. [15] by modifying the scan mode for the experimental S-band radar, named KOUN, at NSSL with long pulses and low antenna rate to enhance the radar measurement capability. Doppler velocities collected with the modified scan mode showed substantially increased coverage in comparison with velocities collected with the unmodified scan mode from the nearby operational test-bed S-band radar, named KCRI. However, since the pulse repetition frequency (PRF) was limited to 455 Hz for the long pulses which reduces the Nyquist velocity to 12.53 m/s for the new scan mode, the collected velocity data with the modified scan mode were severely aliased. The stand-alone version of velocity dealiasing, called SA-VD [16, 17], was tried first to overcome the involved difficulties. Since this SA-VD applies the alias-robust variational method, called AR-Var [18], to low-PRF scanned raw velocities from KOUN to produce the reference velocities for dealiasing, it can overcome the encountered difficulties for some cases but not all the cases. The SA-VD was then modified by using external reference velocities from KCRI to overcome the remaining difficulties in dealiasing. This amounts to a pseudo-dual-PRF approach which was proposed and implemented in Xu et al. [15] with encouraging results. In particular, the pseudo-dual-PRF approach was shown to be effective and able to enhance the dealiased radial-velocity data coverage in comparison with that from KCRI radar and thus also increase the depth covered by the vertical profile of horizontal velocity produced from the dealiased radial-velocity data.

As a follow-up of Xu et al. [15], this paper designs a real dual-PRF scan mode for KOUN, by modifying the aforementioned pseudo-dual-PRF approach, to collect Doppler velocities in pre-storm environments without using external reference velocities from KCRI. The collected velocity data in May 2019 reveal greatly enhanced clear-air data coverage but encounter newly increased difficulties in dealiasing as the environmental flows become strong, complex and very turbulent (so the raw radial velocities are severely aliased and become very noisy). To overcome the increased difficulties, the dealiasing technique [15] must be further improved. In particular, the AR-Var used in the dealiasing technique must be modified and applied to low-PRF scans with its produced reference radial velocities (used as the seed data for the subsequent continuity check) to cover large range circles beyond those covered by high-PRF scans. As will be shown in this paper, such a modification can be done and the modified AR-Var can produce reliable reference radial velocities from low-PRF scans.

The paper is organized as follows. The next section presents the real dual-PRF scan mode designed for KOUN and shows the dual-PRF scanned radial velocity images scanned from KOUN under clear-air weather conditions in pre-storm environments. Section 3 shows the problems and examines the difficulties encountered when the previous dealiasing technique [15] is applied to the raw velocities from KOUN low-PRF scans. Section 4 describes the improved dealiasing technique with the refined AR-Var, and applies it to dual-PRF radial velocities scanned from KOUN to produce dealiased radial velocities with greatly enhanced data coverage free of alias errors. Discussions follow in section 5.

2. Dual-PRF Scan Mode

As explained in Xu et al. [15], the WSR-88Ds are capable of transmitting long (4.5 μs) and short (1.5 μs) pulses with the maximum PRFs of 455 and 1280 Hz respectively due to transmitter duty cycle limitations. The long pulse mode has greater sensitivity than the short pulse mode, but at the cost of a smaller Nyquist velocity, denoted by V_N. In clear air situations, the WSR-88Ds operate in two Volume Coverage Patterns (VCPs): VCP31 uses long pulses while VCP32 uses short pulses. To cover the maximum specified range of 460 km in VCP31, the KOUN radar operates at a PRF of 321 Hz with a Nyquist velocity of $V_N \approx 11$ m/s. To maximize the Nyquist velocity in the long pulse mode, a new experimental low-PRF scan with a PRF of 460 Hz is designed for KOUN. The Nyquist velocity at this low-PRF scan is improved to 12.74 m/s. With the azimuthal scan rate reduced to 2 deg/s for this low-PRF scan, the unambiguous radial range is 326 km, the time per sweep scan is 180 s, and the dwell time is 180 + 2 = 182 s/sweep (with 2 seconds needed to change the tilt) which is longer than the dwell time of 72 (79) s/sweep used by VCP31 (VCP32) for contiguous Doppler scans. This low-PRF scan is coupled with a high-PRF scan (with a PRF of 1200 HZ, azimuthal scan rate of 12 deg/s, time per sweep scan of 30 s, dwell time of 32 s/sweep and V_N of 33.24 m/s) to form a dual-PRF scan mode that couples a high-PRF Doppler-velocity scan with a low-PRF Doppler-velocity scan on each of the three elevation angles from 0.5° to 1.5° and 2.5°). A volume scan is therefore composed of two sub-volume scans: one high-PRF sub-volume scan completed in 3 × 32 = 96 s and one low-PRF sub-volume scan completed in 3 × 182 = 546 s, so the combined volume scan is completed in 96 + 546 = 642 s = 10.7 min. The update time of 10.7 min is slightly longer than that (9 min 50 s) of VCP31 and VCP32 but still sufficiently rapid to resolve the temporal variations of wind fields on the mesoscale, especially in clear air situations. As the high-PRF sub-volume is scanned first (from 0.5°

to 1.5° and then to 2.5° tilt) and followed by its paired high-PRF sub-volume scan (also from 0.5° to 1.5° and then to 2.5° tilt), the time differences between the paired low and high PRF scans completed on 0.5°, 1.5° and 2.5° tilt are 3 × 32 + 182 = 278 s = 4.63 min, 2 × 32 + 2 × 182 = 428 s = 7.13 min and 32 + 3 × 182 = 578 s = 9.63 min. respectively. These time differences can be reduced to 30 + 180 = 210 s = 3.5 min by pairing the low and high PRF scans between two consecutive sweeps on each tilt. Nevertheless, pairing the low and high PRF scans between two consecutive sub-volumes is used in this paper because it can be implemented on the experimental KOUN radar more conveniently than pairing between two consecutive sweeps. Detailed specifications of this dual-PRF scan mode are listed in Table 1.

Table 1 Specifications of dual-PRF scan mode. Here, V_N stands for Nyquist velocity and R_{uam} stands for the unambiguous range.

Coupled sub-volume	Elevation angle (deg)	Pulse length	PRF (Hz)	Samples (#)	Azimuthal rate (deg/s)	Time per sweep (s)	V_N (m/s)	R_{uam} (km)
	0.5, 1.5 or 2.5	Short	1200	100	12	30	33.24	125
		Long	460	230	2.0	180	12.74	326

Figure 1 shows the images of raw radial-component velocities collected from KOUN by using the dual-PRF scans at three elevation angles in a pre-storm environment on 05/09/2019. As shown in panels (a)-(c) of Figure 1, the low-PRF scans at 0.5°, 1.5° and 2.5° can cover disk areas of about 200, 120 and 75 km radii, respectively, while the high-PRF scans at 0.5°, 1.5° and 2.5° can cover disk areas of about 120, 80 and 50 km radii, respectively, as shown in (d)-(f) of Figure 1. Clearly, the low-PRF scans have much larger velocity data coverages than the high-PRF scans, but the low-PRF scanned raw velocities were extensively aliased due to the reduced V_N (from 33.24 to 12.74 m/s). In particular, as marked by white A letters in Figure 1a, the low-PRF scanned raw velocities were aliased extensively in many patch-areas in the northeast (or southwest) quadrant around and beyond 100 km radial range from the radar site where the radial-component velocities of the environmental flow were strongly positive away from the radar (or negative toward the radar), because the environmental flow was southwesterly and westerly and became strong around and above 1 km height – the height of radar beam on 0.5° tilt at 100 km radial range.

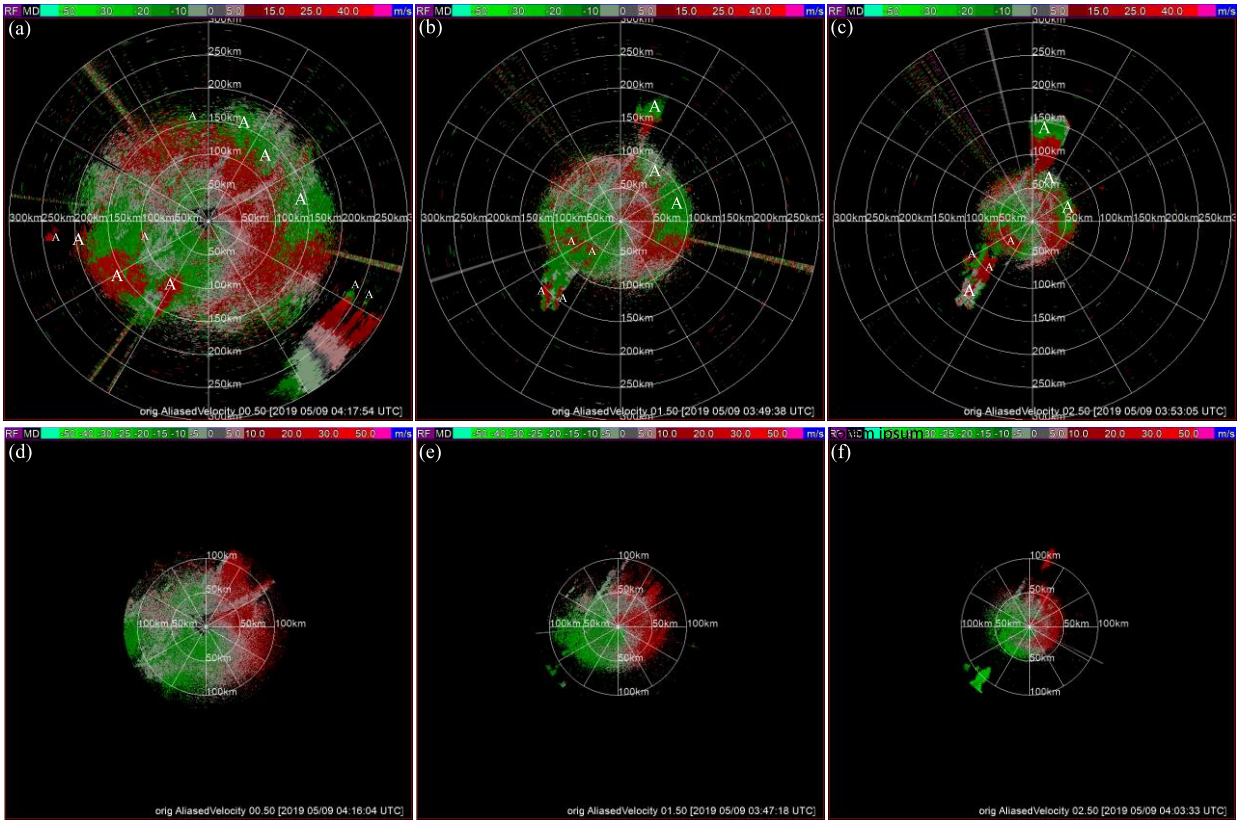

Figure 1 (a) Image of raw radial-component velocities from KOUN low-PRF scan at 0.5° in a pre-storm environment around 04 UTC on 05/09/2019. **(b)** As in (a) but at 1.5°. **(c)** As in (a) but at 2.5°. **(d)** As in (a) but from KOUN high-PRF scan at 0.5°. **(e)** As in (d) but at 1.5°. **(f)** As in (d) but at 2.5°. In panels (a)-(c), white "A"s mark aliased-velocity areas.

Figure 2 shows the images of raw radial-component velocities collected from KOUN by using the dual-PRF scans at three elevation angles in a pre-storm environment on 05/23/2019. As shown in panels (a)-(c) of Figure 2, the low-PRF scans at 0.5°, 1.5° and 2.5° can cover disk areas up to 250, 160 and 120 km radii, respectively, while the high-PRF scans at 0.5°, 1.5° and 2.5° can cover disk areas of about 140, 80 and 60 km radii, respectively, as shown in (d)-(f) of Figure 2. Again, the low-PRF scans have much larger velocity data coverages than the high-PRF scans, but the low-PRF scanned raw velocities are extensively and severely aliased due to the reduced V_N (from 33.24 to 12.74 m/s). In particular, as marked by white A (or A-A) letters in Figure 2a, the low-PRF scanned raw velocities were extensively aliased (or doubly aliased) in many patch-areas in the northeast (or southwest) quadrant around and beyond 100 km radial range from the radar site where the radial-component velocities of the environmental flow were strongly positive away from the radar (or negative toward the radar), because the environmental flow was southwesterly and southerly and became strong (or very strong) above 0.5 (or 1) km height – the height of radar beam on 0.5° tilt at 50 (or 100) km radial range. The low-PRF scanned raw velocities in Figure 1 are less severely aliased but noisier than those in Figure 2. The noisy raw velocities in Figure 1 further increase difficulties in dealiasing as shown in the next section.

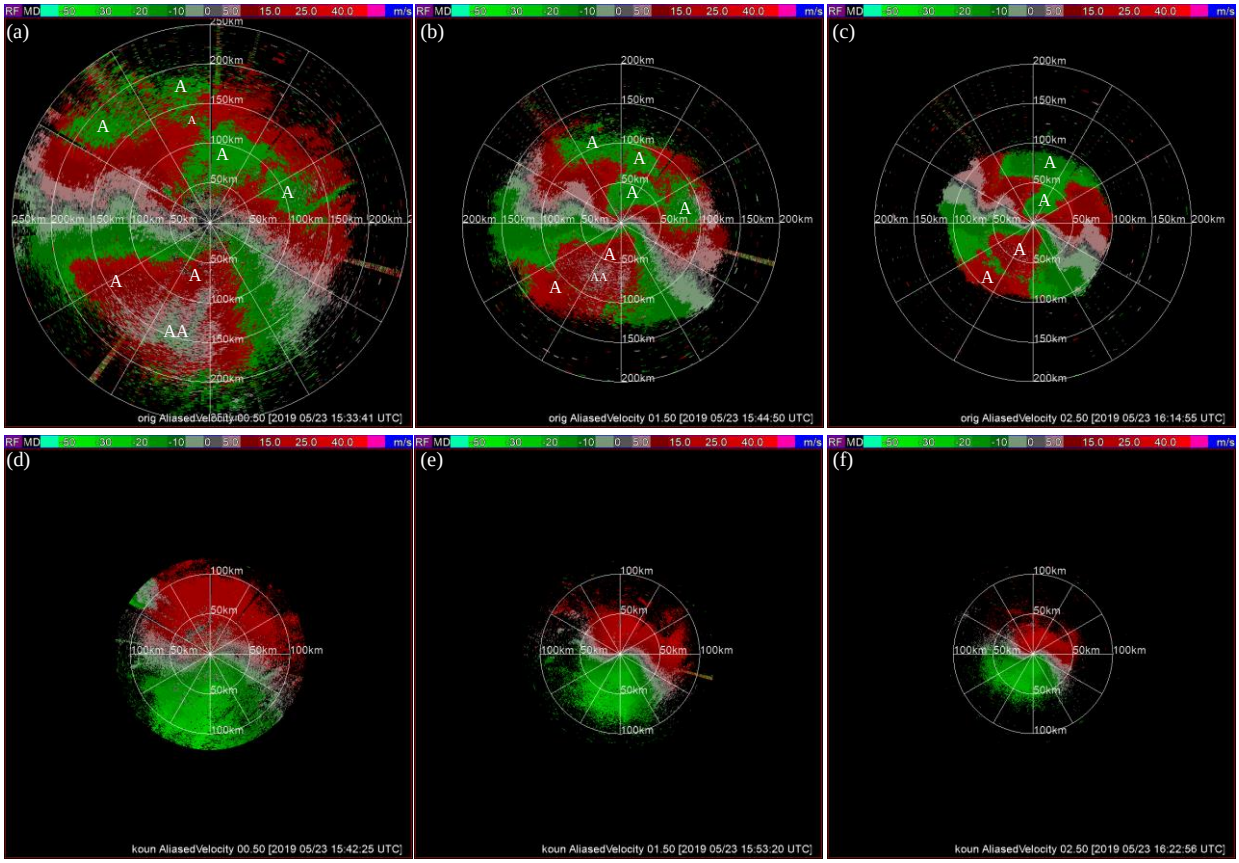

Figure 2 As in Figure 1 but in a pre-storm environment around 16 UTC on 05/23/2019.

3. Problems and Difficulties in Dealiasing

As mentioned in the introduction, the previously developed dealiasing techniques [16, 17] were reduced into a stand-alone version and then modified, by using external reference velocities obtained from KCRI high-PRF scans, to overcome the difficulties in dealiasing the raw velocities from KOUN low-PRF scans in Xu et al. [15]. Although this modified stand-alone dealiasing was applied successfully to dealias the pseudo-dual-PRF velocity data as demonstrated in Xu et al. [15], it encounters further increased difficulties in dealiasing the real-dual-PRF raw velocities, especially when the raw velocities become very noisy. In the case, the continuity check implemented in the last step is no longer error-free when it is applied to raw velocities from low-PRF scan and goes outward beyond the radial range covered by the seed data generated from high-PRF scanned velocities via the reference check (see the flowchart in Figure 16 of Xu et al. [15]).

To illustrate the problem in details, Figure 3a, Figure 3b, Figure 3c plot the images of dealiased velocities produced in the last step by applying the continuity check to the raw velocities from low-PRF scans in Figure 1a, Figure 1b, Figure 1c, respectively, while Figure 3d, Figure 3e, Figure 3f plot the images of seed data generated from high-PRF scanned velocities in Figure 1d, Figure 1e, Figure 1f, respectively. As shown in Figure 3a, Figure 3b, Figure 3c, raw velocities are rejected in many areas (blacked from those in Figure 1a, Figure 1b, Figure 1c) and incorrectly dealiased in areas marked by white "A"s. Data-void areas (in which raw velocities are rejected) and incorrectly dealiased data areas are also seen within the areas covered by the seed data (see Figure 3d, Figure 3e, Figure 3f), and this is because the continuity check goes not only once one-way outward beyond

the radial range covered by the seed data but also subsequently two-way inward-outward several times (see the detailed description in section 3 of Xu et al. [17]) and the inward-going continuity check can "propagate" data-void areas and incorrectly dealiased data areas into the areas of seed data.

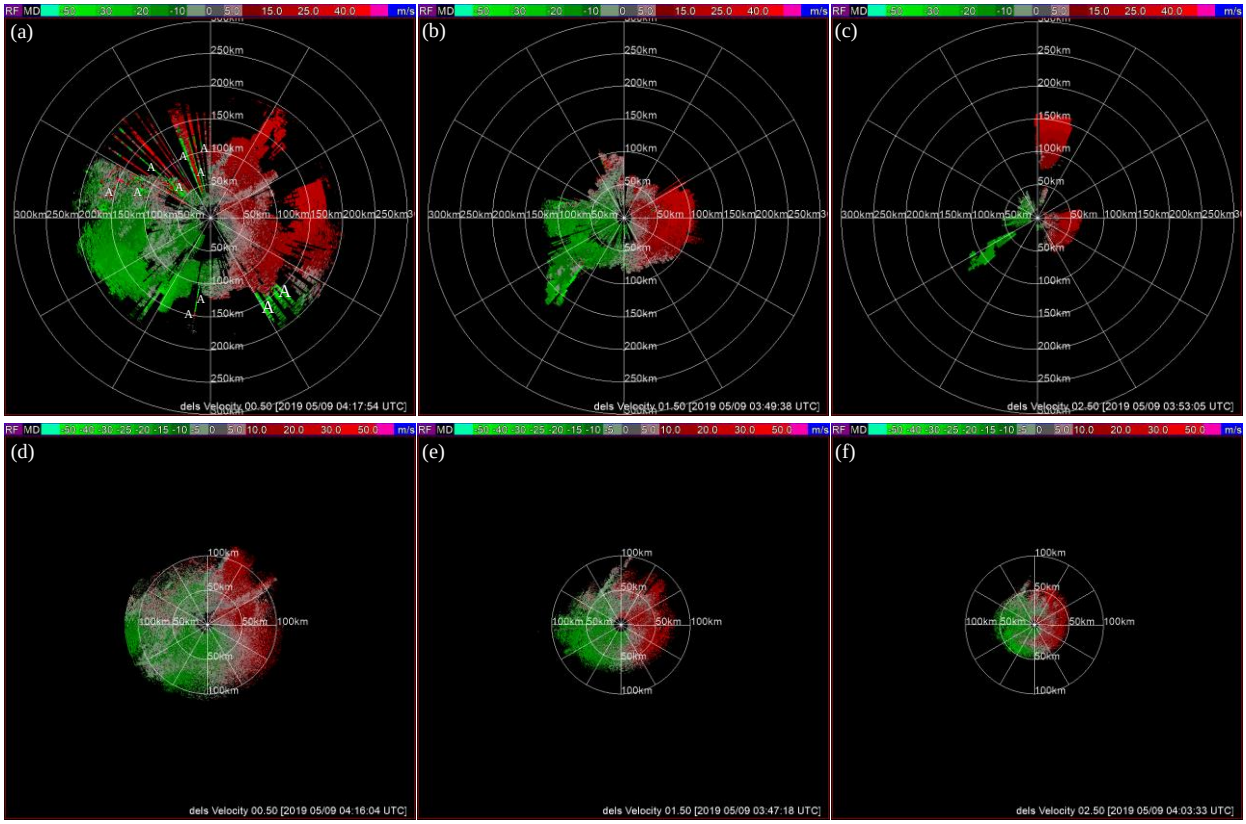

Figure 3 (a) Image of dealiased velocities produced in the last step by applying the continuity check to the raw velocities from low-PRF scan at 0.5° in Figure 1a. **(b)** As in (a) but from low-PRF scan at 1.5° in Figure 1b. **(c)** As in (a) but from low-PRF scan at 2.5° in Figure 1c. **(d)** Image of seed data generated from high-PRF scanned velocities at 0.5° in Figure 1d. **(e)** As in (d) but from high-PRF scanned velocities at 1.5° in Figure 1e. **(f)** As in (d) but from high-PRF scanned velocities at 2.5° in Figure 1f. In panels (a)-(c), white "A"s mark areas of incorrectly dealiased velocities.

On the other hand, as the raw velocities from low-PRF scans in Figure 2a, Figure 2b, Figure 2c are less noisy (though more severely aliased) than those in Figure 1a, Figure 1b, Figure 1c, the dealiased velocities produced by the continuity check in the last step are essentially error-free, as shown in Figure 4a, Figure 4b, Figure 4c, and contain fewer data-void areas (blacked from those in Figure 2a, Figure 2b, Figure 2c). Nevertheless, the data-void areas are also seen within the seed data areas (see Figure 4d, Figure 4e, Figure 4f) and they are again caused by the "propagation" of inward-going continuity check. Thus, the continuity check is still not free of problem in this case.

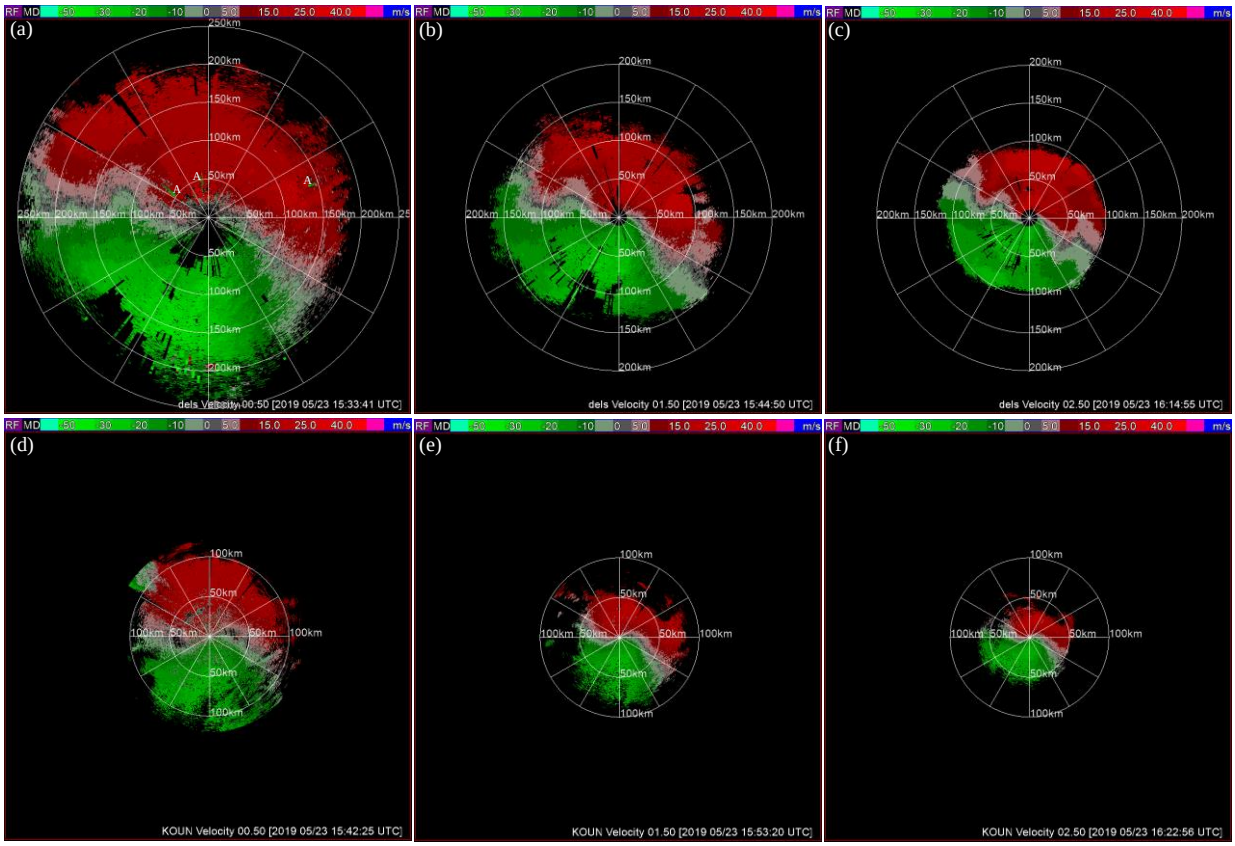

Figure 4 (a) Image of dealiased velocities produced in the last step by applying the continuity check to the raw velocities from low-PRF scan at 0.5° in Figure 2a. **(b)** As in (a) but from low-PRF scan at 1.5° in Figure 2b. **(c)** As in (a) but from low-PRF scan at 2.5° in Figure 2c. **(d)** Image of seed data generated from high-PRF scanned velocities at 0.5° in Figure 2d. **(e)** As in (d) but from high-PRF scanned velocities at 1.5° in Figure 2e. **(f)** As in (d) but from high-PRF scanned velocities at 2.5° in Figure 2f.

4. Improved Dealiasing

To solve the problems and overcome the increased difficulties encountered in dealiasing raw velocities scanned from KOUN using the newly designed real dual-PRF mode, the dealiasing technique proposed for dual-PRF scans (see the flowchart in Figure 16 of Xu et al. [15]) must be improved. Since the problems are caused mainly by the insufficient and limited coverage of seed data produced from high-PRF scans, it becomes desirable and necessary to increase the seed data coverage with additional seed data generated beyond the radial range covered by the seed data generated from high-PRF scanned velocities on each tilt. This can be done by modifying the AR-Var and applying the modified AR-Var to raw velocities from low-PRF scan on each tilt to produce reliable reference radial velocities and then generate seed data beyond the radial range covered by the seed data generated from high-PRF scanned velocities. In this case, an additional step of reference check is performed to produce reliable seed data for the subsequent continuity check going outward, free of error, beyond the radial range covered by the seed data generated from high-PRF scanned velocities on each tilt. The detailed modifications are described/explained below with the AR-Var briefly reviewed first.

The AR-Var was developed originally by Xu and Nai [18] for analyzing highly aliased raw velocities scanned with small Nyquist velocities (≈12 m/s) from winter ice storms in which the environmental flows are quite uniform in the horizontal but strongly sheared in the vertical across each inversion layer. In this AR-Var, the first-guess background radial-velocity field, denoted by v_r^b, is produced on each qualified range circle (which has sufficient raw data coverage) by modifying the alias-robust VAD analysis of Xu et al. [19] and applying the modified AR-VAD, called mod-AR-VAD, to raw velocities scanned with small Nyquist velocities. To be acceptable, v_r^b must fit the raw velocities closely on the qualified range circle (with the fitting residual variance satisfying the stringent threshold condition in (11) of Xu and Nai [18]).

When the mod-AR-VAD is applied to low-PRF scanned raw velocities from KOUN, it often fails to produce acceptable v_r^b because the pre-storm environmental flows are noisier and less horizontally uniform than those in winter ice storms (but the mod-AR-VAD still assumes/requires that the environmental flow are horizontally uniform or nearly so). However, unlike the environmental flows in winter ice storms, the pre-storm environmental flows are not strongly sheared in the vertical, so the analyzed and accepted radial-velocity field, denoted by v_r^a, obtained on the previous range circle (which is slightly smaller and lower than the current range circle) can be used as v_r^b (instead of that produced by the mod-AR-VAD) on the current range circle. This modifies the original AR-Var adaptively for applications to low-PRF scanned raw radial velocities on qualified outer range circles (that is, large range circles not covered by high-PRF scans). This modified AR-Var is named AR-Var-L. On qualified inner range circles (that is, small range circles covered by high-PRF scanned velocities), dealiased radial velocities obtained free of error (via the reference check as shown by the flowchart in Figure 16 of Xu et al. [15]) from high-PRF scanned raw radial velocities (with large Nyquist velocities) can be now used as v_r^b (instead of seed data) to modify the original AR-Var adaptively for applications to low-PRF scanned raw radial velocities on those inner range circles. This modified AR-Var is named AR-Var-S.

When applied to low-PRF scanned raw radial velocities on an entire tilt, the AR-Var-S is used first to produce v_r^a on each qualified and accepted inner range circle, from the smallest to the largest, and then the AR-Var-L is used recursively and sequentially to produce v_r^a on each increasingly large outer range circle. The performance and effectiveness of AR-Var-S (or AR-Var-L) are shown by the example in Figure 5a (or Figure 5c) for a qualified and accepted inner (or outer) range circle within (or beyond) the coverage of high-PRF scan on 0.5° tilt, while Figure 5b shows the performance of AR-Var-S on the largest qualified and accepted inner range circle of r = 85 km marginally covered by the high-PRF scans, where r is the radius of range circle.

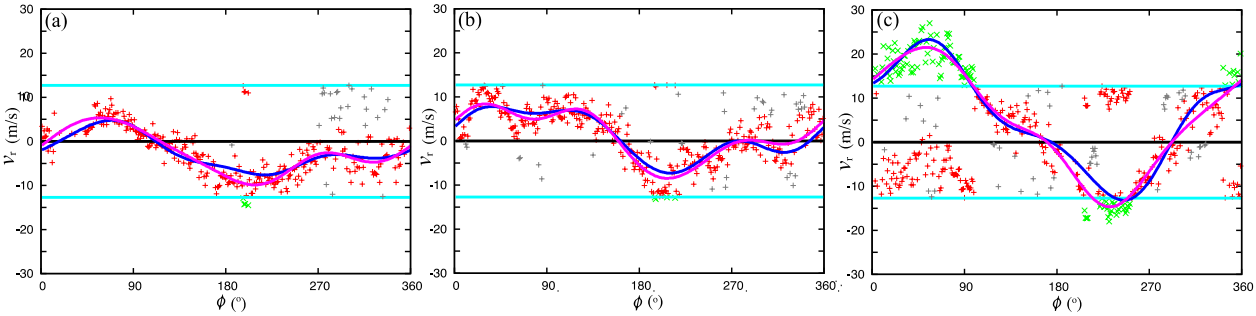

Figure 5 (a) Low-PRF scanned raw radial velocities plotted by red and gray + signs, alias-corrected radial velocities plotted by green × signs, and rejected radial velocities plotted by gray + signs on an inner range circle with r = 35 km < r_{max1} at 0.5° tilt for the case show in Figure 1a, where r is the range circle radius and r_{max1} (=85 km) is the radius of largest qualified and accepted inner range circle covered by the high-PRF scan. The blue curve is the first-guess background radial-velocity field $v_r^b(\Phi)$ given by v_r^a produced from high-PRF scanned raw radial velocities on the same inner range circle (r = 35 km on 0.5° tilt). The purple curve is the analyzed radial-velocity field $v_r^a(\Phi)$ produced by AR-Var-S. The two horizontal cyan lines show the Nyquist range (within $\pm v_N$ = ±12.74 m s^{-1}). **(b)** As in (a) but on the largest inner range circle with $r = r_{max1}$ = 85 km. **(c)** As in (a) but on an outer range circle of r = 150 km with the first-guess background radial-velocity field $v_r^b(\Phi)$ given by the analyzed radial-velocity field $v_r^a(\Phi)$ produced by AR-Var-L on the previous range circle (with r = 150 - 0.5 = 149.5 km), where $r_{max1} < r$ = 150 km < r_{max2} and r_{max2} (=164 km) is the radius of largest qualified and accepted range circle covered by the low-PRF scan.

As shown in Figure 5a, the blue curve of v_r^b (given by the dealiased radial velocities from the high-PRF scan on the same inner range circle) fits closely the retained raw radial velocities (plotted by red + signs except for those aliased and corrected to green × signs) and alias-corrected radial velocities (plotted by green × signs) from the low-PRF scan. Clearly, this blue curve does not fit the analysis-rejected very noisy radial velocities (plotted by gray + signs mainly over the azimuthal range of 270° < Φ < 360°) from the low-PRF scan, but the residual variance of the fitting (to all the original raw radial velocities) is still small enough (to satisfy the stringent threshold condition in (11) of Xu and Nai [18]), so this v_r^b is acceptable. Also, as shown clearly in Figure 5a, the purple curve of v_r^a fits the retained raw radial velocities and the alias-corrected radial velocities more closely and thus can provide reliable reference radial velocities on this inner range circle for the reference check (in an additional step before the continuity check as explained earlier). Similar performances are seen for the AR-Var-S applied to all other qualified and accepted inner range circles, including that shown in in Figure 5b, as an additional example, for the AR-Var-S applied to the largest qualified and accepted inner range circle.

As shown in Figure 5c, the blue curve of v_r^b (given by v_r^a produced from the low-PRF scan on the previous range circle) fits the retained raw radial velocities and alias-corrected radial velocities quite closely on the outer range circle of r = 150 km. Although this blue curve does not fit the analysis-rejected very noisy radial velocities, the fitting residual variance is small enough, so this v_r^b is acceptable. Also as shown in Figure 5c, the purple curve of v_r^a fits the retained raw radial velocities

and alias-corrected radial velocities more closely and thus can provide reliable reference radial velocities on this outer range circle for the reference check.

Using the AR-Var-S and AR-Var-L provided reference radial velocities, the reference check (performed as an additional step) can produce reliable radial-velocity seed data over the entire tilt for the continuity check (to apply, free of error, to the low-PRF scanned raw radial velocities in the last step of dealiasing). This solves the problem and overcomes the difficulties illustrated in section 3, and the dealiasing is improved adaptively. Figure 6 shows the flowchart of this adaptively improved dealiasing algorithm procedure. The satisfactory performances of this improved dealiasing are shown in Figure 7a, Figure 7b, Figure 7c for the low-PRF scanned raw radial velocities in Figure 1a, Figure 1b, Figure 1c. In particular, Figure 7a (Figure 7b or Figure 7c) shows that the reference radial velocities are distributed smoothly on each qualified range circle and the qualified range circles cover the entire 0.5° (1.5° or 2.5°) tilt densely but not continuously (as shown by the blacked narrow circular gaps between densely distributed color circles). Figure 7d (Figure 7e or Figure 7f) shows that the radial-velocity seed data are distributed densely but not continuously (as shown by blacked small arcs of data-void segments) along most qualified range circles on 0.5° (1.5° or 2.5°) tilt. Figure 7g (Figure 7h or Figure 7i) shows that the dealiased radial velocities after the continuity check in the last step are not only free of error but also cover the entire 0.5° (1.5° or 2.5°) tilt more densely than the seed data in Figure 7d (Figure 7e or Figure 7f). The improved dealiasing performs even better when applied to the low-PRF scanned raw radial velocities in Figure 2a, Figure 2b, Figure 2c (which are less noisy than those in Figure 1a, Figure 1b, Figure 1c), and this is illustrated by the results in Figure 8a-Figure 8i.

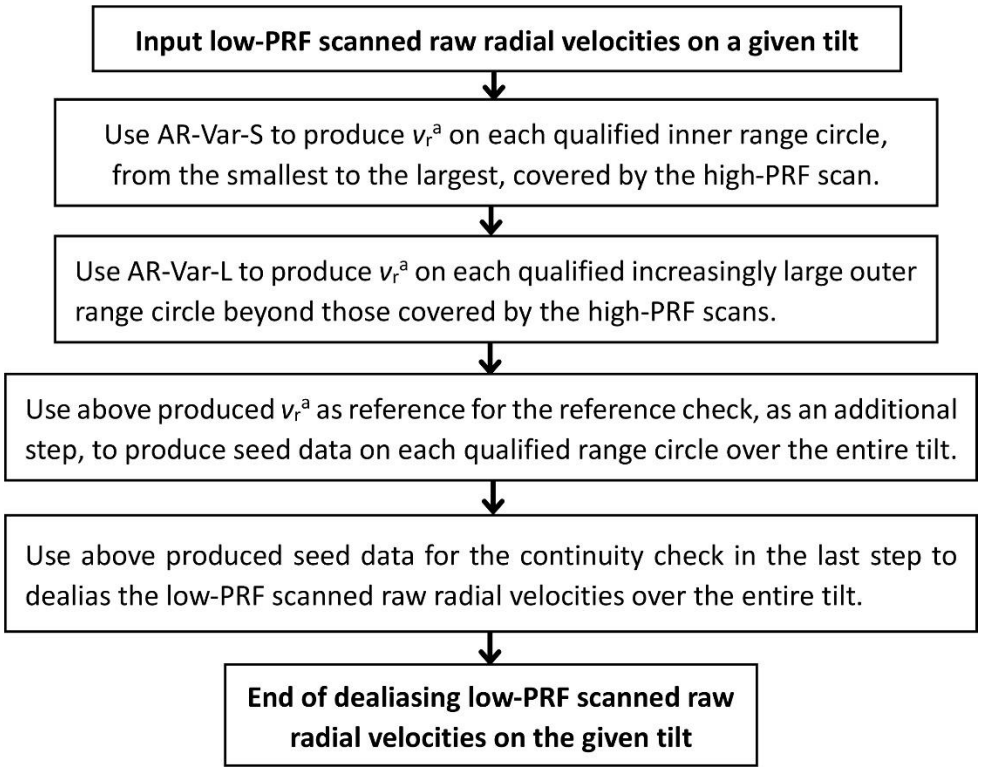

Figure 6 Flowchart of improved dealiasing algorithm procedure for low-PRF scanned raw radial velocities on a given tilt. The improved dealiasing algorithm is computationally efficient as it takes no more than 8 s (CPU time on a workstation) for one tilt.

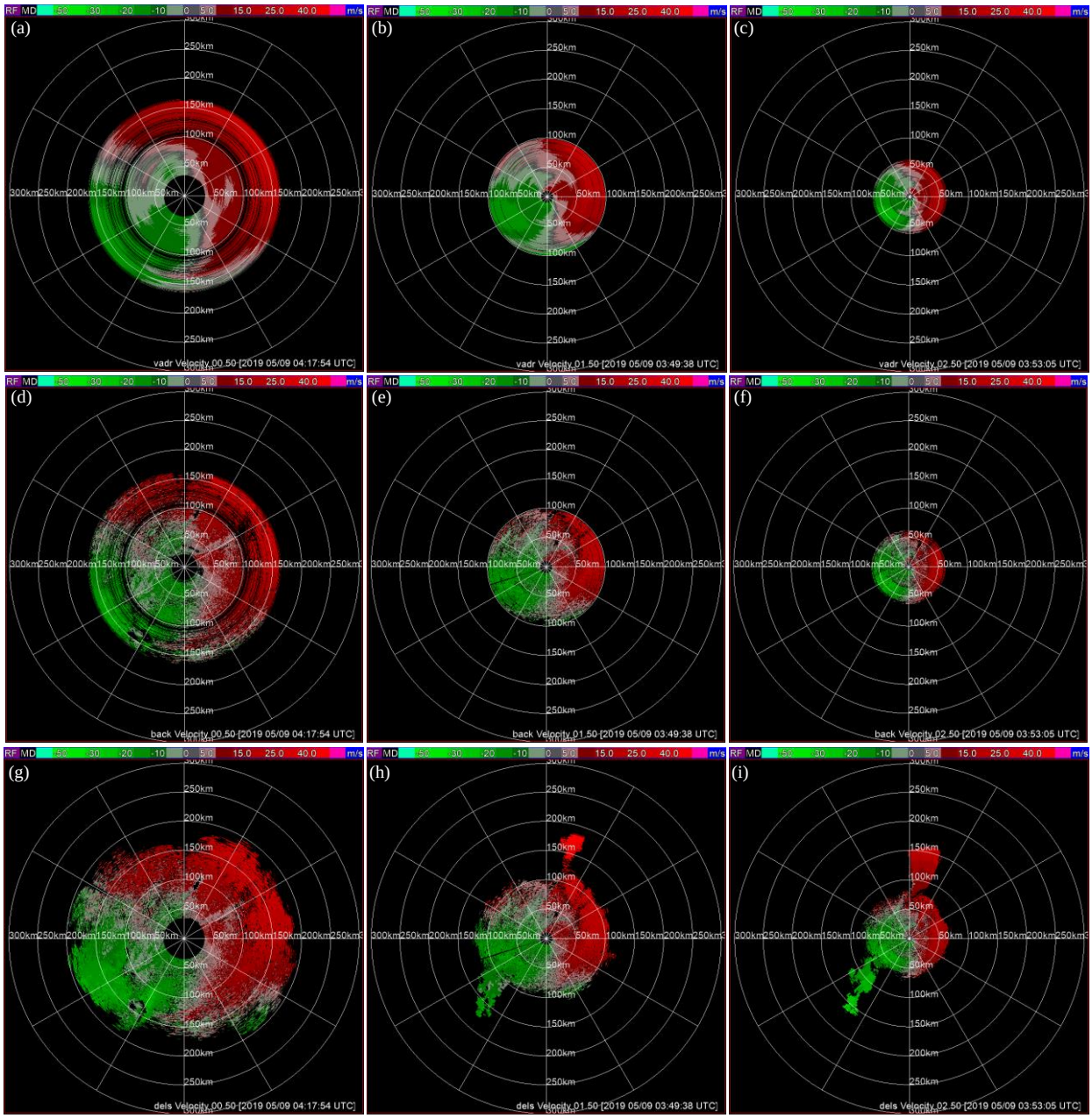

Figure 7 (a) Image of reference radial velocities produced by applying AR-Var-S and AR-Var-L to the raw velocities from low-PRF scan at 0.5° in Figure 1a. **(b)** As in (a) but from low-PRF scan at 1.5° in Figure 1b. **(c)** As in (a) but from low-PRF scan at 2.5° in Figure 1c. **(d)** Image of radial-velocity seed data produced by the additional step of reference check for the raw velocities from low-PRF scan at 0.5° in Figure 1a. **(e)** As in (d) but from low-PRF scan at 1.5° in Figure 1b. **(f)** As in (d) but from low-PRF scan at 2.5° in Figure 1c. **(g)** Image of dealiased radial velocities after the continuity check in the last step for the raw velocities from low-PRF scan at 0.5° in Figure 1a. **(h)** As in (g) but from low-PRF scan at 1.5° in Figure 1b. **(i)** As in (g) but from low-PRF scan at 2.5° in Figure 1c.

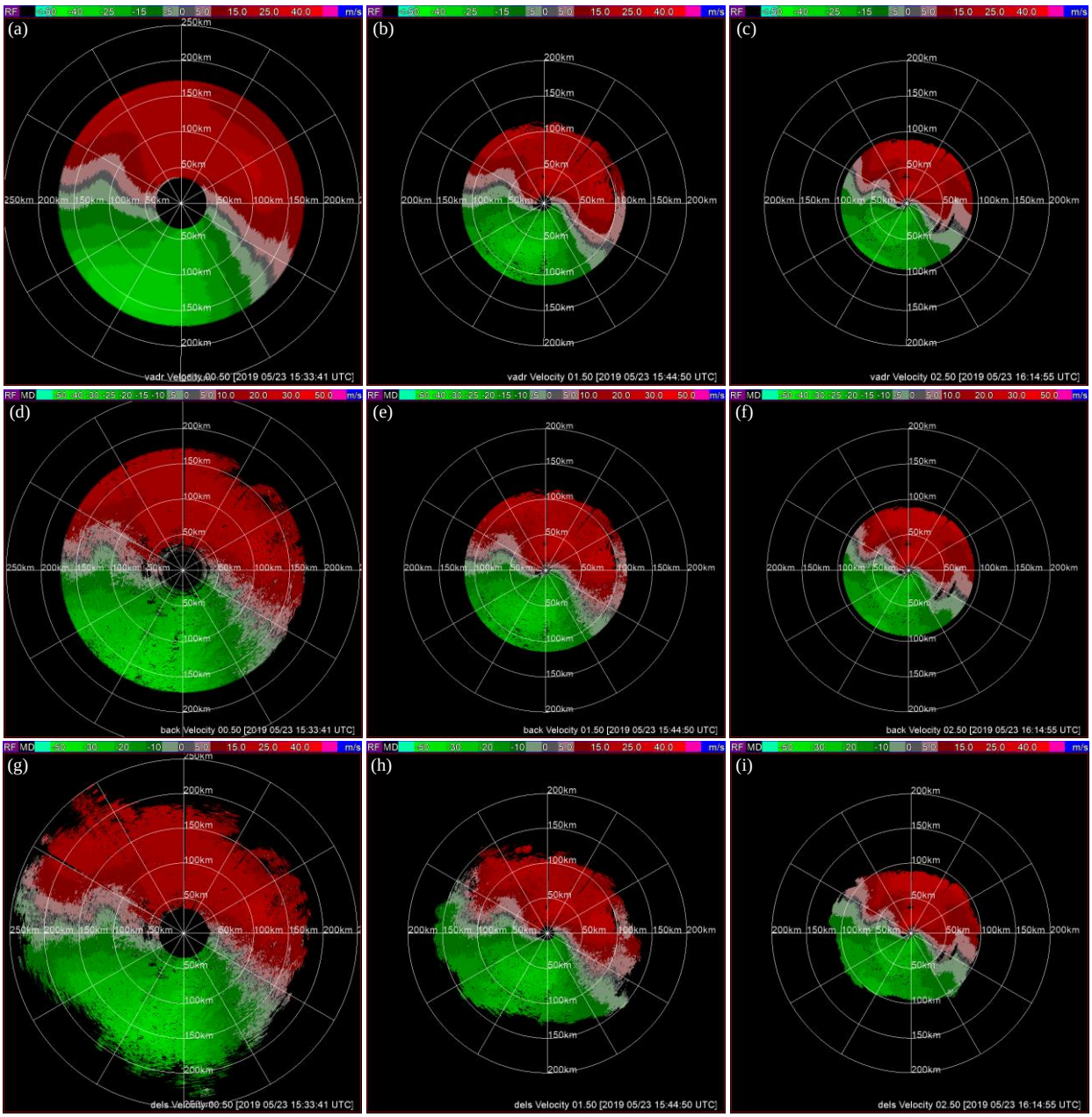

Figure 8 As in Figure 7 but for low-PRF scans in Figure 2a, Figure 2b, Figure 2c.

The skill of improved dealiasing can be measured by the following two percentages in combination: (i) the percentage of retained velocities (including both correctly and incorrectly dealiased velocities) in all the low-PRF scanned raw velocities, and (ii) the percentage of correctly dealiased velocities in all (both correctly and incorrectly) dealiased velocities. These two percentages are calculated and listed, as skill scores, for each case of low-PRF scanned tilt in Table 2. Note that the percentage of rejected velocities is not listed as it is simply 100% minus the percentage of retained velocities. Note also that the number of incorrectly daliased velocities is zero, so the percentage of correctly dealiased velocities is 100% in each case. Thus, as listed in Table 2, the skill score measured by the second percentage is perfect (100%) for all cases. Also, as listed in Table 2, the skill score measured by the first percentage increases as the tilt increases from 0.5° to 1.5° and 2.5° in each sub-volume and as the sub-volume shown in Figure 1a, Figure 1b, Figure 1c changes to that shown in Figure 2a, Figure 2b, Figure 2c. These skill-score increases are consistent

with the detailed results shown in Figure 7 and Figure 8 and can be explained similarly in terms of data noises.

Table 2 Skill scores calculated and measured by (i) the percentage of retained velocities (including both correctly and incorrectly dealiased velocities) in all the low-PRF scanned raw velocities, and (ii) the percentage of correctly dealiased velocities in all (both correctly and incorrectly) dealiased velocities on each of the three tilts in each sub-volume of low-PRF scan. Note that the number of incorrectly daliased velocities is zero, so the percentage of correctly dealiased velocities is 100% in each case.

Case of low-PRF scan	Tilt	Number of all raw velocities	Number (percentage) of retained velocities	Number (percentage) of correctly daliased velocities	Number of incorrectly daliased velocities
Figure 1a	0.5°	128210	90606 (70.7%)	16623 (100%)	0
Figure 1b	1.5°	82018	64816 (79.0%)	10873 (100%)	0
Figure 1c	2.5°	57874	45852 (79.2%)	10230 (100%)	0
Figure 2a	0.5°	137250	107790 (78.5%)	41009 (100%)	0
Figure 2b	1.5°	96134	83908 (87.3%)	31833 (100%)	0
Figure 2c	2.5°	72156	65613 (90.9%)	22931 (100%)	0

5. Discussions

As a follow-up of our previous study [15], a real dual-PRF scan mode is described in this paper for KOUN to collect Doppler velocities in pre-storm environments (without using KCRI). The low-PRF scanned velocities collected by using this dual-PRF scan mode exhibit enhanced clear-air data coverage but encounter new difficulties (caused mainly by the increased data noises) in dealiasing the low-PRF scanned velocities beyond the high-PRF-scan covered radial range. To overcome the difficulties, the AR-Var [18] is modified adaptively and applied to low-PRF scans to produce reference radial velocities for the subsequent continuity check to go, free of error, beyond the high-PRF-scan covered radial range. This improves the dealiasing technique [15] effectively and adaptively, so clear-air velocities collected by using the newly designed real dual-PRF scan mode in pre-storm environments can be processed free of alias errors (and thus usable for wind analyses and data assimilation although these utilities require continued research beyond this paper).

Here, it is necessary to point out that the dual-PRF approach presented in this paper for S-band (10-cm wavelength) Doppler radars is very different from the previous dual-PRF technique, including the commercial dual-PRF processor [20], that has been employed on operational C-band (5-cm wavelength) Doppler radars in Canada, Australia and Europe [21-23] and also on research mobile and airborne Doppler radars [24, 25]. The major differences can be highlighted in the following three aspects:

(i) The previous dual-PRF technique was developed to increase the Nyquist velocity v_N (≈ 13 m/s) for C-band (or X-band) Doppler radars. In particular, v_N can be increased by an integer factor m (=2, 3 or 4) for an initial velocity estimate derived from the difference between low-PRF and high-PRF scanned phase shifts (at two adjacent gates on the same radial-range circle). On the contrary, the current dual-PRF approach is designed to enhance S-band Doppler radar

sensitivity and thus increase the clear-air Doppler velocity data coverage of low-PRF scan but with its Nyquist velocity compromised and reduced (to nearly 12 m/s).

(ii) The previous dual-PRF technique pairs the low and high PRF scans between two adjacent rays, so the azimuthal change of true radial velocity between the paired gates (on two adjacent rays) should not be too large for using the low-PRF and high-PRF scanned phase shifts (at two adjacent gates) to derive the initial velocity estimate (at a single gate). Besides, random measurement errors are doubled as the initial velocity estimate is derived from two independently measured phase shifts. The current dual-PRF approach, however, pairs the low and high PRF scans between two consecutive sub-volumes. Therefore, as a limitation, the temporal change of true radial-velocity field between the two sub-volumes should not be too large for using the analyzed radial-velocity field from the high-PRF scan as the first guess for the AR-Var-S applied to the low-PRF scan.

(iii) The previous dual-PRF technique uses the aforementioned initial velocity estimate only for determining the number of folds that the original velocity estimated at each gate (from high-PRF or low-PRF scan) has undergone within its corresponding v_N. This number of folds is then used to dealias the original velocity to produce the "final" velocity estimate at each gate (without doubling measurement random errors) in the dual-PRF processor. Since the "final" velocity estimates still can have alias errors (at localized points and in clusters in areas of high azimuthal shear of radial velocity), various methods of continuity check (with no preceding reference check) have been developed/employed to detect/correct dual-PRF processor errors via post processing [21-24]. As these methods were developed not for the same purpose/application as considered in this paper, they are very different from the continuity check (see section 3 of Xu et al. [17]) used in the last step for the new dual-PRF approach presented (see Figure 6) in this paper.

The limitation explained in (ii) has not caused a problem for the clear-air dual-PRF data so far collected, but it can cause the AR-Var-S fail (to use the analyzed radial-velocity field from the high-PRF scan as the first guess) if the change of true radial-velocity field between the two consecutive sub-volume scans exceeds $7v_N/4$ (=22.3 m/s) over a large sector (according to the refinement (vi) explained in section 2.3 of Xu and Nai [18]). This limitation can be alleviated by pairing the low and high PRF scans not between two consecutive sub-volumes but between two consecutive sweeps on each tilt to reduce the time difference between the paired low and high PRF scans (from 4.63-9.63 to 3.5 min, as explained in section 2). Besides, the limitation may be also alleviated by adaptively refining the adjustable threshold condition (see (14) of Xu and Nai [18]) for the AR-Var-S. These remedies will be explored/employed in case if the above concerned situation occurs. Another limitation for the improved dealiasing is that gaps in low-PRF scanned velocities cannot be too large between outer range circles (or between isolated data areas) to allow the AR-Var-L (or the continuity check) to go through. So far, this limitation has not caused a serious problem because low-PRF scanned clear-air velocity fields are usually quite continuous.

The two type of adaptively modified AR-Var (named AR-Var-S and AR-Var-L in this paper indicates that the original AR-Var [18] is flexible enough to be modified adaptively for various different types of environmental flows although the AR-Var [18] was developed originally for analyzing aliased raw velocities scanned with small Nyquist velocities (≈12 m/s) from winter ice storms in which the environmental flows are quite uniform in the horizontal but strongly sheared in the vertical across

each inversion layer. Modifications of AR-Var for other types of environmental flows (beyond and in addition to the pre-storm environment flow considered in this paper) deserve continued studies.

Acknowledgments

The authors are thankful to Dr. Pengfei Zhang at NSSL for reviewing the original manuscript internally and to the two anonymous reviewers for their constructive comments and suggestions.

Author Contributions

Motivation and conceptualization: Qin Xu. Dual-PRF scan mode design and data collection: Valery Melnikov. Adaptive Doppler-Velocity Dealiasing: Kang Nai. Adaptive modifications of AR-Var: Qin Xu and Kang Nai. Writing and editing: Qin Xu. All authors have read the manuscript and agreed to submit.

Funding

The research work was supported by the NSSL Warn-on-Forecast project and the Office of Naval Research under Award Number N000142012449 to the University of Oklahoma (OU). Funding was also provided by NOAA/Office of Oceanic and Atmospheric Research under NOAA-OU Cooperative Agreement #NA21OAR4320204, U.S. Department of Commerce.

Competing Interests

The authors have declared that no competing interests exist.

References

1. Crum TD, Saffle RE, Wilson JW. An update on the NEXRAD program and future WSR-88D support to operations. Weather Forecast. 1998; 13: 253-262.
2. Whiton RC, Smith PL, Bigler SG, Wilk KE, Harbuck AC. History of operational use of weather radar by U.S. weather services. Part II: Development of operational doppler weather radars. Weather Forecast. 1998; 13: 244-252.
3. Stumpf GJ, Witt A, Mitchell ED, Spencer PL, Johnson JT, Eilts MD, et al. The national severe storms laboratory mesocyclone detection algorithm for the WSR-88D. Weather Forecast. 1998; 13: 304-326.
4. Simmons KM, Sutter D. WSR-88D radar, tornado warnings, and tornado casualties. Weather Forecast. 2005; 20: 301-310.
5. Lakshmanan V, Smith T, Stumpf G, Hondl K. The warning decision support system–integrated information. Weather Forecast. 2007; 22: 596-612.
6. Hardegree SP, Van Vactor SS, Levinson DH, Winstral AH. Evaluation of NEXRAD radar precipitation products for natural resource applications. Rangel Ecol Manag. 2008; 61: 346-353.
7. Brotzge J, Donner W. The tornado warning process: A review of current research, challenges, and opportunities. Bull Am Meteorol Soc. 2013; 94: 1715-1733.
8. Zhang J, Howard K, Langston C, Kaney B, Qi Y, Tang L, et al. Multi-Radar Multi-Sensor (MRMS) quantitative precipitation estimation: Initial operating capabilities. Bull Am Meteorol Soc. 2016;

97: 621-638.
9. Liu S, DiMego G, Guan S, Kumar VK, Keyser D, Xu Q, et al. WSR-88D radar data processing at NCEP. Weather Forecast. 2016; 31: 2047-2055.
10. Benjamin SG, Weygandt SS, Brown JM, Hu M, Alexander CR, Smirnova TG, et al. A North American hourly assimilation and model forecast cycle: The Rapid Refresh. Mon Weather Rev. 2016; 144: 1669-1694.
11. Stensrud DJ, Wicker LJ, Xue M, Dawson DT, Yussouf N, Wheatley DM, et al. Progress and challenges with Warn-on-Forecast. Atmos Res. 2013; 123: 2-16.
12. Wheatley DM, Knopfmeier KH, Jones TA, Creager GJ. Storm-scale data assimilation and ensemble forecasting with the NSSL experimental Warn-on-Forecast System. Part I: Radar data experiments. Weather Forecast. 2015; 30: 1795-1817.
13. Lawson JR, Kain JS, Yussouf N, Dowell DC, Wheatley DM, Knopfmeier KH, et al. Advancing from convection-allowing NWP to Warn-on-Forecast: Evidence of progress. Weather Forecast. 2018; 33: 599-607.
14. Yussouf N, Wilson KA, Martinaitis SM, Vergara H, Heinselman PL, Gourley JJ. The coupling of NSSL warn-on-forecast and flash systems for probabilistic flash flood prediction. J Hydrometeorol. 2020; 21: 123-141.
15. Xu Q, Nai K, Melnikov V. A new radar scan mode to increase clear-air velocity data coverage and usability for wind analysis. J Atmos Ocean Technol. 2019; 36: 1105-1125.
16. Xu Q, Nai K. An adaptive dealiasing method based on variational analysis for radar radial velocities scanned with small Nyquist velocities. J Atmos Ocean Technol. 2012; 29: 1723-1729.
17. Xu Q, Nai K, Liu S, Karstens C, Smith T, Zhao Q. Improved doppler velocity dealiasing for radar data assimilation and storm-scale vortex detection. Adv Meteorol. 2013; 2013: 562386.
18. Xu Q, Nai K. A two-step variational method for analyzing severely aliased radar velocity observations with small Nyquist velocities. Q J R Meteorol Soc. 2013; 139: 1904-1911.
19. Xu Q, Nai K, Wei L. Fitting VAD wind to aliased Doppler radial-velocity observations: A global minimization problem with multiple minima. Q J R Meteorol Soc. 2010; 136: 451–461.
20. RVP 6 Doppler signal processor user's manual. Westford: Sigmet Inc.; 1997. p. 218.
21. Joe P, May PT. Correction of dual PRF velocity errors for operational Doppler weather radars. J Atmos Ocean Technol. 2003; 20: 429-442.
22. Holleman I, Beekhuis H. Analysis and correction of dual PRF velocity data. J Atmos Ocean Technol. 2003; 20: 443-453.
23. Altube P, Bech J, Argemí O, Rigo T, Pineda N, Collis S, et al. Correction of dual-PRF Doppler velocity outliers in the presence of aliasing. J Atmos Ocean Technol. 2017; 34: 1529-1543.
24. Addison Alford A, Biggerstaff MI, Ziegler CL, Jorgensen DP, Carrie GD. A method for correcting staggered pulse repetition time (PRT) and dual pulse repetition frequency (PRF) processor errors in research radar datasets. J Atmos Ocean Technol. 2022; 39. doi: 10.1175/JTECH-D-21-0176.1.
25. Jorgensen DP, Shepherd TR, Goldstein AS. A dual-pulse repetition frequency scheme for mitigating velocity ambiguities of the NOAA P-3 airborne Doppler radar. J Atmos Ocean Technol. 2000; 17: 585-594.

Enjoy *JEPT* by:

1. Submitting a manuscript
2. Joining in volunteer reviewer bank
3. Joining Editorial Board
4. Guest editing a special issue

For more details, please visit:
http://www.lidsen.com/journal/jept